Flight-like critical-angle transmission grating x-ray performance for Arcus

Ralf K. Heilmann[a], Alexander R. Bruccoleri[b], Vadim Burwitz[c], Peter Cheimets[d], Casey DeRoo[e], Alan Garner[f], Eric M. Gullikson[g], Hans Moritz Günther[f], Gisela Hartner[c], Edward Hertz[d], Andreas Langmeier[c], Thomas Müller[c], Surangkhana Rukdee[c], Thomas Schmidt[c], Randall K. Smith[d], and Mark L. Schattenburg[a]

[a]Space Nanotechnology Laboratory, MIT Kavli Institute for Astrophysics and Space Research, Massachusetts Institute of Technology, Cambridge, MA 02139, USA
[b]Izentis, LLC, Cambridge, MA 02139, USA
[c]Max-Planck-Institut für Extraterrestrische Physik, 85748 Garching, Germany
[d]Center for Astrophysics, Harvard-Smithsonian Astrophysical Observatory, Cambridge, MA 02138, USA
[e]University of Iowa, Iowa City, IA 52242, USA
[f]MIT Kavli Institute for Astrophysics and Space Research, Massachusetts Institute of Technology, Cambridge, MA 02139, USA
[g]Lawrence Berkeley National Laboratory, Berkeley, CA 94720, USA

ABSTRACT

High resolving power soft x-ray spectroscopy has been confirmed by the recent Astro2020 Decadal Survey as a high-priority strategic goal with $R = \lambda/\Delta\lambda$ as high as 7500 for some science cases. Examples are the characterization of highly ionized gases in galaxy halos and within and around galaxy clusters, accretion onto supermassive black holes, coronal mass ejections and coronal heating. Below the level of an expensive strategic mission, but far exceeding current capabilities, falls the Arcus Grating Explorer mission concept, with a minimum R of 2500 (expected $R = 3500$) and effective area up to ~ 300 cm^2 in the 12-50 Å bandpass. Arcus relies on light-weight, high-efficiency, blazed and alignment-insensitive critical-angle transmission (CAT) gratings for dispersion. The mission calls for hundreds of $\sim 30 \times 30$ mm^2 gratings with a hierarchy of integrated support structures. The most recent CAT gratings have been fabricated from 200 mm silicon-on-insulator wafers using commercial, volume production compatible tools from the semiconductor and MEMS industries. We report x-ray results from quasi-fully illuminated, co-aligned CAT gratings showing record-high $R \sim 1.3 \times 10^4$ in 18$^{\text{th}}$ order at Al-K$_\alpha$ wavelengths, and diffraction efficiency of blazed orders in agreement with pencil beam synchrotron measurements and model predictions at O-K. Tilt of the deep-etched, freestanding grating bars relative to the grating surface is measured and successfully compensated through angular alignment during bonding of the Si gratings to metal frames. We also report on updates to the Arcus resolving power error budget, and on post-fabrication thinning of grating bars, which could lead to increased diffraction efficiency.

Keywords: Arcus, critical-angle transmission grating, x-ray spectroscopy, blazed transmission grating, soft x ray, grating spectrometer, high resolving power

1. INTRODUCTION

The Astro2020 Decadal Review, "Pathways to Discovery in Astronomy and Astrophysics",[1] endorsed three broad science themes: "Worlds and Suns in Context," "New Messengers and New Physics," and "Cosmic Ecosystems." High resolution and high sensitivity spectroscopy in the soft x-ray band, covering the characteristic lines of C, N,

---

O, Ne and Fe ions, is an essential technique that contributes to all three of these themes. We cite a few themes from the Decadal Review here:

In the area of low-mass stars and how they affect their surroundings and exoplanet formation, "increases in throughput by two or more orders of magnitude, and increases in spectral resolution by factors of 2 to 5, will open up discovery space through measurements of thermal broadening and new line-ratio diagnostics," and also "studies of quiescent and/or lower energy phenomena, such as coronal heating and absorption of [coronal mass ejections (CME)], would benefit from high spectral resolution at lower [x-ray] energies; these can be obtained with grating spectrometers."[1] Furthermore, "the higher energy radiation (UV and X ray) from low mass stars can also drastically alter the chemistry of planetary atmospheres, and thus the habitability of planets, but more precise determinations are needed of how the relevant radiation changes as a function of stellar mass or age".[1]

Dust in the interstellar medium (ISM) plays a critical role in the formation of molecular clouds, and the varying dust-to-gas ratio throughout the ISM leads to variations in this role. Future needs are "observations of X-ray absorption fine structure from elements/minerals in dust and gas using 0.2–2 keV spectroscopy with high resolution ($R \sim 3000$) and 10–100× larger effective collecting area than current facilities".[1]

The structure of our universe is determined by dynamics playing out over a vast range of length scales, from the cosmic web connecting galaxy clusters, through galaxy halos, the ISM, and down to compact objects (accreting supermassive black holes, binary systems, stars) and their winds (jets, CMEs). Today's baryonic structure is the result of a complex dance between infalling and ejected matter across these length scales. As an example, "perhaps the biggest puzzle lies in understanding the subtle problem of the co-existence of gas at very different temperatures and densities in the [galactic] outflows".[1] A key technique to characterize this warm-hot intergalactic medium (WHIM) is high-resolution soft x-ray absorption line spectroscopy, using AGN sightlines as backlights.[2,3] Diffraction grating spectrometers are currently the only feasible technique for high-resolution spectroscopy in the soft ($E < 2$ keV) x ray band. X-ray microcalorimeters (XMC) have a fixed energy resolution (~ 5 eV for XRISM;[4] ~ 2 eV for Lynx[3]), while only critical-angle transmission (CAT) x-ray grating spectrometers (XGS) have repeatedly demonstrated record-high $R \sim 10^4$ at ~ 1.5 keV in the lab.[5–7]

Significant advances in grating technology have been made over the last decade and a half. In contrast, older in-plane reflection grating (XMM-Newton)[8] and gold transmission grating (Chandra)[9] technologies were developed a generation ago, and the instruments have aged in the harsh space environment since 1999.

CAT gratings are blazed transmission gratings. A CAT-XGS combines the benefits of transmission gratings – low mass, volume and power (for thermal control), relaxed alignment and stability tolerances, reduced part count – with those of blazed reflection gratings (use of higher diffraction orders, which boosts spectral resolving power $R = \lambda/\Delta\lambda$). In addition, CAT gratings are transparent at higher energies and thus able to pass useful x rays to a detector (CCD or XMC) at the telescope focus.

Arcus is a proposed grating spectrometer Explorer that addresses many of the above high priority science themes. It consists of four parallel optical channels (OC). Each channel has a sub-apertured array of 12 m-focal-length silicon pore optics (SPO),[10] followed by an array of CAT gratings arranged on a tilted Rowland torus.[11,12] Multiple blazed orders and the 0th order image from each OC get collected by two shared CCD readout arrays. Arcus is expected to provide effective area up to $A_{eff} \sim 300$ cm^2 in the 1.2-5 nm bandpass with $R > 2500$ (requirement) or higher, with a goal of $R \sim 3500$. This will exceed the spectroscopic figures of merit for Chandra and XMM-Newton by factors of 5-10. Due to the gratings' partial transparency, additional significant effective area between 150 and 800 cm^2 in 0th order with CCD energy resolution (~ 70 eV) in the ~ 1.5-6 keV range could be achievable.

To realize an instrument achieving this performance, over 500 CAT grating facets $\sim 30 \times 30$ mm^2 in area each have to be fabricated. Over the last few years we have gradually transferred grating fabrication steps to high-volume and 200 mm-wafer-compatible commercial lithography, coating, and etching tools from the semiconductor and MEMS industries.[7] These tools produce the silicon membranes that contain the CAT grating bars. The membranes are aligned and bonded to flexured metal frames, comprising a grating facet.

In this work we present x-ray results from the first few flight-like Arcus grating facets fabricated with high-volume tools and aligned with some of the methods proposed for flight hardware production. We continue to refine the Arcus resolving power and alignment error budget and present recent updates. One of the ways to

increase the diffraction efficiency of CAT gratings is to make the grating bars thinner. However, thinner bars are more easily damaged during the most forceful fabrication steps (piranha cleaning, etc.) We present early results from a gentle bar thinning process that can be applied at the very end of fabrication to freestanding gratings.

2. CAT GRATING PRINCIPLE AND STRUCTURAL HIERARCHY

CAT gratings feature ultra-high aspect-ratio, freestanding grating bars with nm-smooth sidewalls.[13] They are inclined such that x rays of wavelength λ impinge on the sidewalls at graze angles θ below the critical angle for total external reflection θ_c (see Fig. 1). The diffraction angle β_m for the mth diffraction order is given by the grating equation

$$\frac{m\lambda}{p} = \sin\theta - \sin\beta_m, \tag{1}$$

where p is the grating period. Diffraction orders near the direction of specular reflection from the sidewalls show increased efficiency (i.e., blazing). The small critical angles for soft x rays (typically on the order of 1-2 degrees) demand high-aspect ratio grating bars in order to intercept all incoming photons. Furthermore, we want the bars to be as thin as possible to minimize blockage and absorption. The grating period cannot be too large compared to the x-ray wavelength to obtain diffraction orders that can be sorted by order using the energy resolution of Si-based detectors. We initially chose a design with grating period $p = 200$ nm, grating bar depth $d = 4$ micrometers, and bar thickness $b \approx 60$ nm. Recently we demonstrated $d > 5.5$ μm.[14] Blazing is most efficient when $\tan\theta \approx (p-b)/d$. (For $d = 4$ μm this means $\theta \approx 2$ deg.)
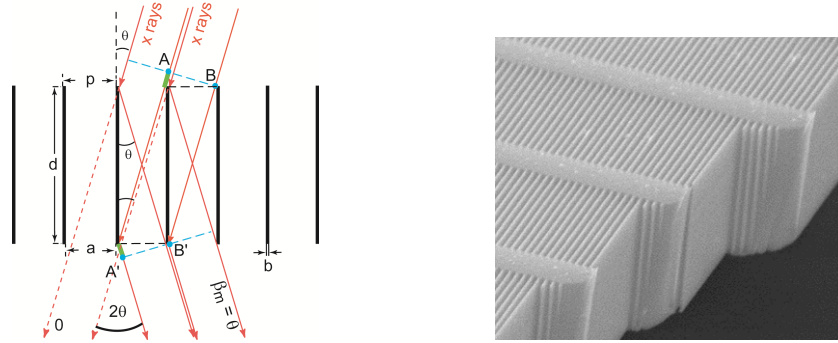

Figure 1. Left: Schematic cross-section through a CAT grating of period p. The mth diffraction order occurs at an angle β_m where the path length difference between AA' and BB' is $m\lambda$. Shown is the case where β_m coincides with the direction of specular reflection from the grating bar sidewalls ($|\beta_m| = |\theta|$), i.e., blazing in the mth order. Right: Scanning electron micrograph (SEM) of a cleaved CAT grating membrane showing top, cross-section and sidewall views of the 200 nm-period silicon grating bars and their monolithically integrated 5 μm-period L1 cross supports (x rays enter from the top and leave out the bottom).

CAT grating bars are not supported by a membrane, but freestanding. As seen on the right in Fig. 1, the bars are held in place by a monolithically integrated 5 μm-period Level 1 (L1) support mesh. Additional support structures are needed for the few-μm thin grating layer in order to manufacture large enough CAT gratings that can cover large areas on the order of thousands of square centimeters with a reasonable number of gratings. Fig. 2 shows an additional, much thicker and stronger Level 2 (L2) hexagonal support structure on the scale of ~ 1 mm. The photograph on the right shows a so-called silicon grating membrane, etched from an silicon-on-insulator (SOI) wafer and featuring an additional 2 mm-wide Level 3 (L3) frame around the edge.

It would be impractical and expensive to try to build a large ($\sim 0.5 \times 0.5$ m^2) array of aligned grating membranes from silicon. Instead, each Si membrane is epoxy-bonded in four spots on the L3 frame to a flexured Ti frame, comprising a grating facet. The Ti frame is then mechanically fastened to a grating window, holding six aligned facets. For Arcus, each OC has a grating petal, which is populated by 24 grating windows. In the end
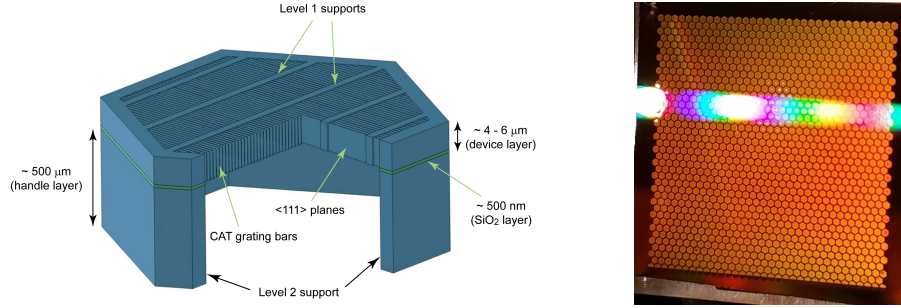
Figure 2. Left: Schematic showing the structural hierarchy of a CAT grating membrane (not to scale). Right: Photograph of an existing 32 x 32 mm² CAT grating membrane with back illumination to show the hexagonal L2 mesh, and with visible light diffraction due to the L1 mesh.

all 144 grating membranes in the OC will be held tangentially to the same tilted Rowland torus within certain alignment tolerances.[11, 12]

3. X-RAY PERFORMANCE OF FLIGHT-LIKE GRATING FACETS

We have recently produced several flight-like grating facets.[15] The grating membranes were made from 200 mm silicon-on-insulator (SOI) wafers, mostly using tools that are compatible with the volume production of CAT gratings.[7] "Flight-like" here means having the same dimensions (32×32.5 mm²) and frame design as planned for Arcus. There are only two differences with respect to the Arcus baseline parameters. First, due to optical proximity effects during the 4X optical projection lithography (OPL) step the L1 bars ended up being 1.1 instead of 0.75 μm wide. This will be corrected with the next OPL mask. Second, some of the gratings were made from SOIs with thicker device layers ($d > 5.5$ instead of 4 μm). Deeper gratings are more challenging to fabricate, but offer the potential for higher diffraction efficiency.[14]

Four grating membranes were selected for bonding to frames. For three of them we had previously measured diffraction efficiency in small spots at beamline 6.3.2 at the Advanced Light Source (ALS), an x-ray synchrotron at Lawrence Berkeley National Laboratory.[14]

3.1 Bar Tilt Correction

The ultra-high aspect ratio grating bars are primarily sculpted in a deep reactive-ion etch (DRIE) step. This etch is not perfectly normal to the SOI device layer surface, but can deviate from normal by a few tenths of a degree or more. The deviations are generally smaller in later generation DRIE tools and near the center of large wafers. We measure this so-called bar tilt using a combination of small-angle x-ray scattering (SAXS) and laser reflection.[16] Each Si membrane is then rotated by its average measured bar tilt in the appropriate direction (grating yaw, the same angle as θ in Fig. 1), such that after bonding the grating bars are (on average) parallel to the facet frame normal. See Fig. 3 for a schematic depiction.
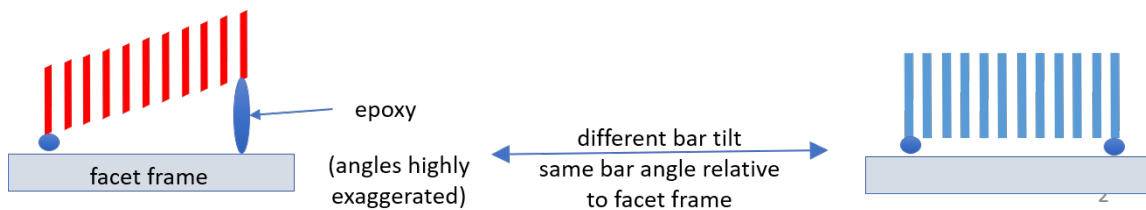

Figure 3. Schematic showing the idea for bar tilt adjustment through epoxy bonding. On the right is a membrane with grating bars parallel to the membrane surface normal. No yaw adjustment is necessary. On the left is a membrane where the grating bars are at a known non-zero angle relative to the surface normal. The membrane is rotated in yaw relative to the facet frame and held with the grating bars parallel to the facet frame normal while the epoxy cures.

3.2 Grating Window

We designed a grating window to hold four grating facets in Arcus-like fashion. Unfortunately, due to schedule delays the window only became available a very short time before the x-ray tests at the PANTER x-ray facility in Germany, and it turned out to be out of specifications. The four grating facets were mounted to the window without metrology feedback. The gratings are labelled CNS1, CNS5, SEG25, and SEG30 (see Fig. 4). The CNS gratings nominally have $d = 4$ μm, and the SEG gratings nominally have $d = 6$ μm.
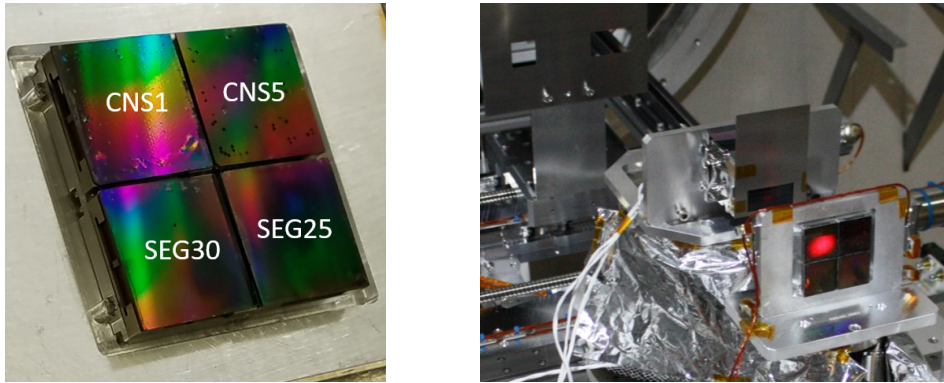

Figure 4. Left: Photograph of the 2×2 grating window, populated with four grating facets. Right: Setup at PANTER during laser alignment. Facet CNS1 is illuminated by the alignment laser coming through the SPO ca. 100 mm upstream from the grating window. Mask apertures can be seen further upstream. See Heilmann et al.[15] for details.

3.3 Grating Roll

Relative grating roll U (rotation about the grating surface normal) was not controlled during mounting of the grating facets to the grating window. At PANTER we used an alignment laser from the position of the x-ray source to diffract red light from the L1 support mesh for one grating facet at a time. Since there is a lithographically defined fixed angle (90 degrees) between L1 bars and CAT grating bars we can use L1 diffraction to measure the relative roll angles between the CAT grating dispersion directions of the four different mounted facets. These laser-based roll measurements, performed with measuring tape, showed that gratings SEG25 and SEG30 only differed by $\Delta U = U_{SEG25} - U_{SEG30} = -1.5$ arcmin, with an estimated measurement uncertainty of 5 arcmin. Gratings CNS1 and CNS2 had ΔU of 33 arcmin and -52 arcmin, respectively. After the x-ray measurement campaign we deduced ΔU from the relative camera pixel coordinates of x-ray diffraction peaks and camera translation stage positions. We found $\Delta U = -1.7 \pm 0.4$ arcmin (SEG25), 28.4 ± 0.5 arcmin (CNS1), and -52.8 ± 0.6 arcmin (CNS5) relative to SEG30, showing good agreement with the laser-based measurements within uncertainties.[15]

3.4 Compensating for Bar Tilt: X-ray Measurements of Relative Grating Yaw

The average bar tilts for the four grating membranes had a standard deviation of ~ 14 arcmin (1σ) from the group average. Uncompensated, this would significantly exceed the currently budgeted tolerance of 9 arcmin (3σ). Relative grating yaw was measured at PANTER using Al-K x rays by performing a yaw scan on 0th order for each bonded grating facet. The center of symmetry of the yaw scan data is at the yaw angle where the the CAT grating bars - averaged over the x-ray footprint - are parallel to the incident x rays. We found relative yaw angles of -10, -12, -13, and -15 arcmin for the four grating facets, resulting in a standard deviation of 1.8 arcmin from the average. Hence, the bar tilt adjustment process described in Fig. 3 resulted in an almost 10-fold improvement, bringing the facets well within the budgeted tolerance.[15]

3.5 Effective Grating Resolving Power

We measured the effective grating resolving power at PANTER in a fashion described in more detail elsewhere.[6, 15] Briefly, we look at the 18th order of the Al-K$_\alpha$ doublet, projected onto the grating dispersion axis, and compare

Table 1. Fit results for effective resolving power R_G for all four gratings and for the partial combination of SEG25 and SEG30.

Grating	best fit R_G	upper bound (3σ)	lower bound (3σ)
CNS1[a]	8.1×10^3	2.6×10^4	5.3×10^3
CNS5[a]	6.9×10^3	1.3×10^4	4.9×10^3
SEG25[b]	1.3×10^4	3.2×10^4	9.4×10^3
SEG30[b]	9.3×10^3	1.1×10^4	8.1×10^3
SEG25/30	1.3×10^4	∞	8.2×10^3

[a] Nominally 4 μm-thick device layer. [b] Nominally 6 μm-thick device layer.

it to its theoretical (natural) width. The doublet is broadened due to the point-spread function (PSF) of the illuminating optic (in this case a silicon pore optic or SPO),[10] the angular size of the x-ray source, and the pixel size of the x-ray detector. The combination of these three terms is measured ("direct beam" DB), modelled as a Gaussian, and the FWHM and Gaussian width σ_{DB} in the dispersion direction are obtained. We model the measured doublet shape as a convolution of the natural shape with a Gaussian of fitted width σ_f, and assume that it can be described as

$$\sigma_f^2 = \sigma_G^2 + \sigma_{DB}^2 \ , \tag{2}$$

where σ_G is conservatively assigned to broadening caused by the illuminated grating. Based on Eq. 1, σ_G can be converted into grating period variations Δp. Assuming a Gaussian period distribution with FWHM Δp, we define $R_G = p/\Delta p$ as the effective grating resolving power and derive a conservative lower limit for R_G from the fit to the data.

All four gratings were measured individually, and SEG25 and SEG30 were also measured simultaneously, with the optic centered between them. Out of the 28×28.5 mm^2 grating area, $\sim 28 \times 22.3$ mm^2 was illuminated by the SPO. Fig. 5 shows examples of the measured spectral shapes along with model fits.
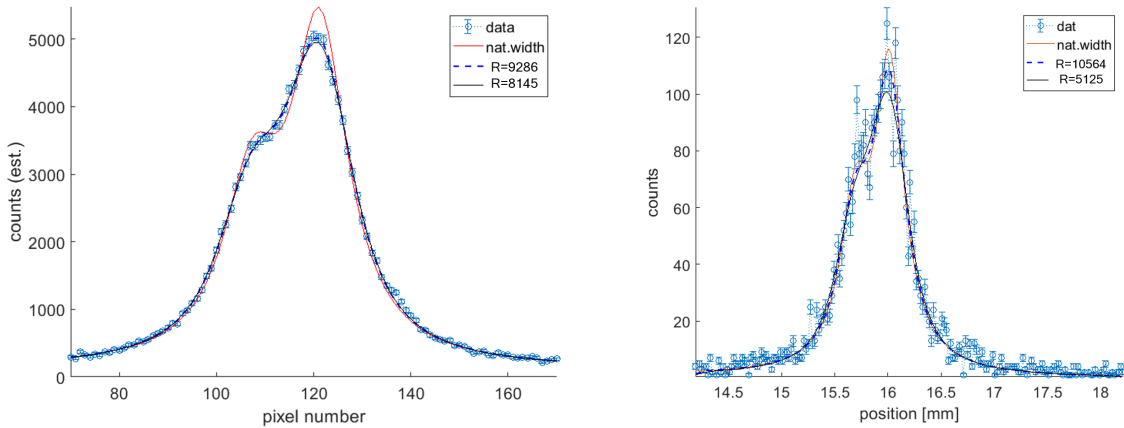

Figure 5. Left: Al-K$_\alpha$ doublet in 18$^{\text{th}}$ order from grating SEG30. Shown are the estimated number of Al-K photons as a function of detector pixel column number (20 μm/pixel). The red line is the natural line shape of the doublet and the dashed line is the best fit to the data. The black solid line is the curve for the lower 3σ confidence limit, corresponding to $R_G = 8145$. Right: Similar for grating SEG25 in 21$^{\text{st}}$ order, as a function of position on the detector. More details are given elsewhere.[15]

Table 1 lists the best fit results for R_G and the upper and lower 3σ bounds, showing best fits between $R_G = 6.9 \times 10^3$ and 1.3×10^4. We were also able to measure 21$^{\text{st}}$ order with a second camera at the same time as

18$^{\text{th}}$ order. Count rates for the higher order were lower, which led to wider 3σ intervals, but the best fit values for R_G agreed well with 18$^{\text{th}}$ order results within uncertainties.[15]

The resolving power for a fully populated Arcus OC has many terms besides the R_G values of the individual gratings, and the Arcus team maintains error budgets for all relevant terms for two scenarios: required performance (RP) and current best performance estimates (CBE) for all terms. The requirement of $R \geq 2500$ is met if all gratings deliver $R_G \geq 4100$ in the RP scenario, and $R_G \geq 2900$ in the CBE scenario. Our results show that all four tested gratings safely exceed this performance by factors between 1.7 and 4.6.[15]

3.6 CAT Grating Diffraction Efficiency

Grating diffraction efficiency at wavelength λ in order m is most easily defined as the flux measured in m^{th} order divided by the (monochromatic) flux of the same wavelength incident on the grating. For CAT gratings with their hierarchy of support structures we must pay attention to the illuminated area, and whether it contains L1, L2, or L3 support structures. And in order to estimate efficiency at wavelengths between the measured ones we need a theoretical model for diffraction efficiency. We have used rigorous coupled-wave analysis (RCWA)[17] with good success for many years to model diffraction efficiency for CAT grating structures of the type shown in Fig. 1.[7,18] In synchrotron experiments, however, the x-ray beam footprint extends over many tens to hundreds of micrometers and covers many L1 periods. Therefore L1 absorption and diffraction must be taken into account. For Arcus 144 grating facets per OC will be practically fully illuminated, including L2 and L3 structures. Due to the size and thickness of these structures they can simply be treated as absorbers.

At PANTER individual gratings had $\sim 78\%$ of their area (inside the L3 frame) illuminated by a single SPO, which means both L1 and L2 effects have to be considered. We used a silicon oxide target to generate characteristic O-K radiation, held each grating at the nominal Arcus angle of $\theta = 1.8$ degrees, and measured count rates for the direct beam from the SPO (no grating in the path), 0$^{\text{th}}$ order (grating centered on the SPO beam, but camera at the direct beam position), and diffracted orders $m = 4$-7. Seventh order was included in our measurements since we could reach it with the camera, even though the Arcus readouts will only collect orders 4-6 at O-K. Unfortunately we ran out of time before we could perform a complete set of measurements for grating CNS5.

Diffraction efficiency of grating membranes CNS1, SEG25, and SEG30 had been measured at the ALS at a wavelength of 2.38 nm, near the peak of the broad O-K spectrum, with a small beam footprint that easily fit within a single L2 hexagon. In our recent analysis we took into account the different experimental configurations (source spectrum, beam size, detector aperture, effects of L1 and L2 structures, detector physics, etc.) to compare synchrotron and PANTER data, and confirmed that the results agree with each other within measurement uncertainties.[15] Comparing these results with the CAT grating model for Arcus ($d = 4$ μm, $b = 60$ nm, see Fig. 1) that underlies current effective area predictions, we find that the sum of efficiencies from orders 4-7 (23.7% - 28.3%, including L1 and L2 absorption) meets or exceeds the model value of 22.9% for all three grating facets.[15]

4. RESOLVING POWER/ALIGNMENT ERROR BUDGET

When we talk about the Arcus resolving power at a given wavelength we mean the average of the resolving power of the recorded blazed diffraction peaks, weighted by their relative effective areas.[11] Many terms contribute to the resolving power of an Arcus OC: point spread functions and alignment of the individual SPOs, effective resolving power and alignment of the individual CAT grating facets, distribution of effective area between the blazed diffraction peaks, and alignment of the readout camera relative to the surface of best focus.[12] Many of these contributors have both static and dynamic terms, and there are additional purely dynamic contributors (e.g., pointing reconstruction errors, jitter). We have investigated the sensitivities of many of these elements and their impact on resolving power and effective area in the past using ray tracing. From these results we assigned initial error budgets to individual terms, based on reasonable estimates and feasibility. As we gain feedback from our experiments we continue to revisit the error budget and look for places where we can relax it without impacting performance.

4.1 Grating Rotational Tolerances

As an example, we have relaxed rotational alignment tolerances for CAT grating membranes and/or facets to their grating window from previous, overly conservative assigned values.[12] Fig. 6 shows the result of ray trace simulations where we use the relaxed values of 15 arcmin (3σ) for grating roll (rotation around the grating normal, which rotates the dispersion axis) and 9 arcmin (3σ) in yaw (rotation around the grating bars, which affects the blaze angle). The error budget for grating pitch is also held at 15 arcmin (3σ), but performance is much less sensitive to pitch than to yaw and could be relaxed further. In the ray trace all possible alignment tolerances are varied at the same time according to the alignment budget. The alignment budget assumes that all alignment tolerances contribute independently and the simulations here are designed to check this assumption. Some misalignments might cancel out in practice, others might have a multiplicative effect. Full ray tracing is the best way to check this and to predict final instrument performance.
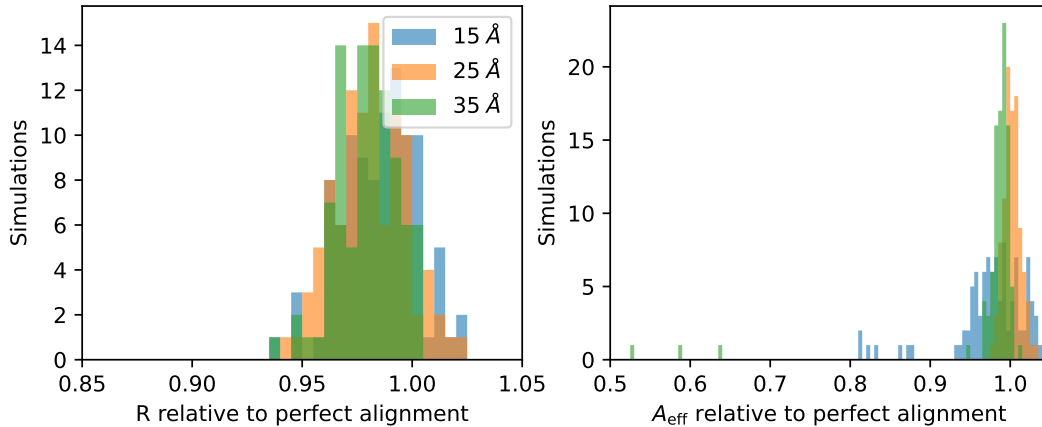

Figure 6. Histogram of ray trace results with relaxed error budgets for grating rotational misalignments for three different wavelengths. See text for details.

As can be seen in Fig. 6, the loss in R is about 2% relative to perfect alignment of all components ($R = 3500$-4000), and there is no obvious reduction in effective area. ("Outliers" occur when a specific diffraction order lands on a chip gap.) This is not visibly different from the results for the previous tighter error budget.[12] Further relaxation may be possible or desirable, even if R or A_{eff} are impacted slightly, but other advantages are gained in exchange (schedule, cost, etc.).

4.2 Yaw Tolerance for Bar Tilt Adjustment

In the ray trace results above, grating bars are assumed to be parallel to the grating normal, as shown on the right in Fig. 3. The grating yaw alignment error budget is primarily constrained due to its impact on A_{eff}, since the wrong grating bar sidewall angle could blaze x rays into orders that do not fall onto the readout. However, as we have pointed out in Section 3.1, the DRIE generally is not perfectly normal to the Si wafer surface. The question arises, how far the etch can deviate from normal, before the subsequent bar tilt correction during bonding - which reinstates the correct blaze orientation - has a negative impact on R, since it can lead to increased deviation of the grating surface from the surface of the ideal Rowland torus.

The practical implications of this question are how much bar tilt we can tolerate from the DRIE step. Bar tilt is generally small near the center of a wafer, and increases toward the edges. The tilt behavior can be fine-tuned to an extent in modern DRIE tools, but it is not a trivial task. The more tilt we can tolerate by correction during bonding, the larger the surface of a 200 mm wafer is that we can use for gratings. We currently assume to only use four gratings from the center of each wafer, but increasing this number (up to as many as 24) could lead to significant cost and schedule savings.

This question is also best addressed with ray tracing. In Fig. 7 we assume that each grating has a random value of bar tilt between -0.4 and +0.4 degrees, which then is adjusted within the above yaw tolerance of 9

arcmin (3σ) for improved blazing. As expected, proper blazing leads to practically optimal A_{eff}, but at the small cost of a slight additional 2% reduction in R relative to Fig. 6.
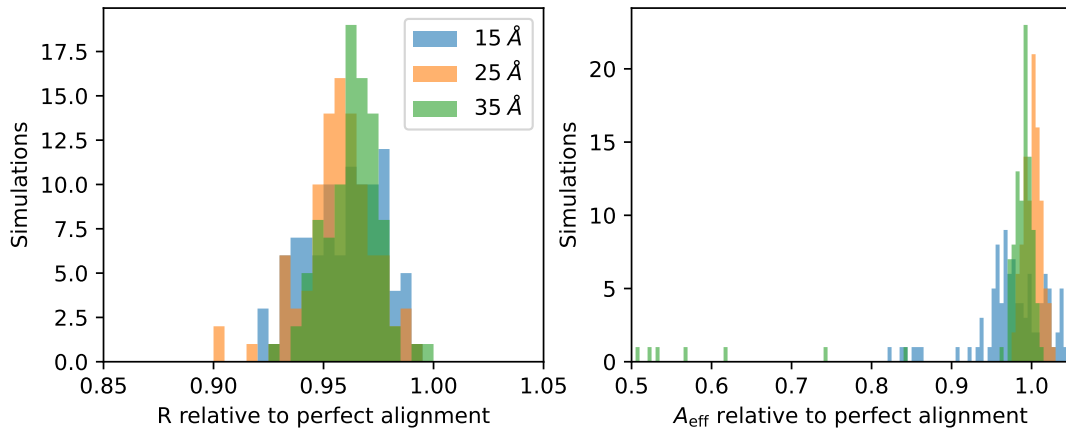

Figure 7. Histogram of ray trace results with compensated bar tilts in the range of -0.4 to + 0.4 degrees for three different wavelengths. See text for details.

5. POST-FABRICATION GRATING BAR THINNING

As can be seen in Fig. 1, the thinner the grating bars are, i.e., the smaller b is, the more x rays will hit the grating bar sidewalls and contribute to diffraction efficiency instead of being absorbed. There is a lower physical limit, since for $b \lesssim 10 - 15$ nm, soft x rays start to tunnel through the grating bars and blazing is reduced. Our current gratings have $b \sim 50 - 70$ nm, and trying to make them thinner lowers the fabrication yield, mostly in the last few wet (piranha) cleaning steps when the grating bars are already freestanding, at their thinnest, and therefore the most vulnerable. Ideally we would keep the bars somewhat thicker (~ 100 nm) throughout the current fabrication procedure, and make them thinner afterward.

We have begun to investigate a gentle, vapor-based process to thin the grating bars that can be applied at the very end of fabrication. A native oxide layer automatically forms on silicon surfaces at room temperature in ambient air, where oxygen penetrates into the top few Si layers to form oxide, "consuming" some of the silicon. The width of the non-oxidized Si part of the grating bar is thereby reduced slightly. We remove the native oxide using HF vapor, resulting in a slightly thinner bar. Over the course of a day or so a native oxide layer will reform, which we then remove again with HF vapor. As a proof of concept, we have repeated this process 30 times, and observed thinning at a rate of ~ 1.4 nm/cycle (see Fig. 8). While native oxide formation is slow, the oxidation/HF vapor cycle could be automated and performed with many dozens of gratings at once with minimal human intervention. Alternatively, we plan to investigate process parameters (temperature, oxygen concentration, etc.) that could speed up oxidation and grow thicker oxide layers, leading to faster and fewer cycles.

6. DISCUSSION AND OUTLOOK

We have fabricated multiple flight-like CAT grating facets using methods and tools compatible with volume manufacturing. Grating bar tilt was measured and successfully corrected during the facet bonding step, as verified with x rays at the PANTER facility. Four flight-like grating facets, made from three different 200 mm SOI wafers, were assembled into a 2×2 grating window and almost-fully illuminated in the converging beam of an Arcus-like SPO. All four gratings demonstrated effective resolving power 2-4 times higher than required for Arcus, with $R_G = 6.9 \times 10^3$ to 1.3×10^4. Two of the grating facets were partially illuminated simultaneously, and their combined spectrum gave $R_G \approx 1.3 \times 10^4$, demonstrating that well-aligned CAT grating arrays can be made without a reduction in resolving power.
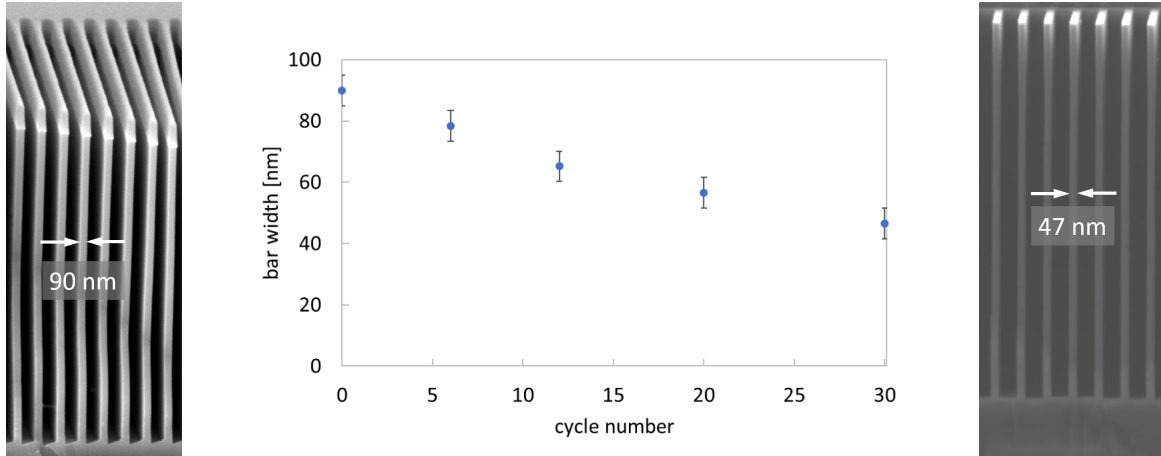
Figure 8. Bar thinning through repeated oxidization and HF vapor etching. Left: SEM of a cleaved CAT grating structure after DRIE and KOH polish. Middle: Bar width derived from SEMs as a function of the number of oxide growth/HF vapor etch cycles. Right: SEM of a cleaved grating after 30 oxidization/HF vapor cycles. The bars are visibly thinner but remain intact.

The three gratings we were able to test at PANTER for diffraction efficiency at O-K wavelengths in an Arcus-like configuration showed performance in agreement with previous synchrotron spot measurements and - after taking into account the slightly wider than planned L1 bars - with model predictions for Arcus effective area.

We have started the process of producing new gratings for future testing. In the past we could only obtain 200 mm SOIs with device layer thickness (i.e., d) tolerances of ± 1 μm over the area of a wafer. This can lead to overetching (undercutting and detachment from the buried oxide layer) or underetching (leftover Si between the grating bars) at the same time in different areas of a wafer and reduces fabrication yield. We have recently identified a new vendor and obtained a set of 200 mm SOIs with a device layer thickness tolerance of ± 0.1 μm, which should practically eliminate yield losses due to this issue.

The Arcus error budget continues to be refined using experience gathered from our experiments and extensive ray tracing. We also continuously work on fabrication process improvements to increase yield and reduce costs. Repeated oxidization/vapor HF cycles can be used to gently reduce the CAT grating bar width and potentially increase diffraction efficiency. We plan to explore how thin we can go before the bars break on their own or fail under environmental testing. Future x-ray measurements on thinner bars will be essential to verify that the sidewalls do not become rougher during these cycles, which could lead to reduced efficiency. On the other hand, these cycles might reduce sidewall roughness, in which case efficiency is expected to increase.

In summary, CAT grating technology and manufacturability have matured greatly over the last decade and a half. We are confident that CAT grating technology is ready to support a successful Arcus mission.

ACKNOWLEDGMENTS

REFERENCES

[1] National Academies of Sciences, Engineering, and Medicine, "Pathways to Discovery in Astronomy and Astrophysics for the 2020s," (2021).

[2] Smith, R. and Arcus Team, "The Arcus soft x-ray grating spectrometer Explorer," in [*SPACE TELE-SCOPES AND INSTRUMENTATION 2020: ULTRAVIOLET TO GAMMA RAY*], DenHerder, J., Nikzad, S., and Nakazawa, K., eds., *Proceedings of SPIE* **11444**, SPIE (2021). Conference on Space Telescopes and Instrumentation - Ultraviolet to Gamma Ray / SPIE Astronomical Telescopes + Instrumentation Conference, DEC 14-18, 2020.

[3] Gaskin, J. A., Swartz, D. A., Vikhlinin, A., Ozel, F., Gelmis, K. E., Arenberg, J. W., Bandler, S. R., Bautz, M. W., Civitani, M. M., Dominguez, A., Eckart, M. E., Falcone, A. D., Figueroa-Feliciano, E., Freeman, M. D., Guenther, H. M., Havey, K. A., Heilmann, R. K., Kilaru, K., Kraft, R. P., McCarley, K. S., McEntaffer, R. L., Pareschi, G., Purcell, W., Reid, P. B., Schattenburg, M. L., Schwartz, D. A., Schwartz, E. D., Tananbaum, H. D., Tremblay, G. R., Zhang, W. W., and Zuhone, J. A., "Lynx x-ray observatory: an overview," *JOURNAL OF ASTRONOMICAL TELESCOPES INSTRUMENTS AND SYSTEMS* **5** (APR 2019).

[4] Tashiro, M., Maejima, H., Toda, K., Kelley, R., Reichenthal, L., Hartz, L., Petre, R., Williams, B., Guainazzi, M., Costantini, E., Fujimoto, R., Hayashida, K., Henegar-Leon, J., Holland, M., Ishisaki, Y., Kilbourne, C., Loewenstein, M., Matsushita, K., Mori, K., Okajima, T., Porter, F. S., Sneiderman, G., Takei, Y., Terada, Y., Tomida, H., Yamaguchi, H., Watanabe, S., Akamatsu, H., Arai, Y., Audard, M., Awaki, H., Babyk, I., Bamba, A., Bando, N., Behar, E., Bialas, T., Boissay-Malaquin, R., Brenneman, L., Brown, G., Canavan, E., Chiao, M., Comber, B., Corrales, L., Cumbee, R., de Vries, C., den Herder, J.-W., Dercksen, J., Diaz-Trigo, M., DiPirro, M., Done, C., Dotani, T., Ebisawa, K., Eckart, M., Eckert, D., Eguchi, S., Enoto, T., Ezoe, Y., Ferrigno, C., Fujita, Y., Fukazawa, Y., Furuzawa, A., Gallo, L., Gorter, N., Grim, M., Gu, L., Hagino, K., Hamaguchi, K., Hatsukade, I., Hawthorn, D., Hayashi, K., Hell, N., Hiraga, J., Hodges-Kluck, E., Horiuchi, T., Hornschemeier, A., Hoshino, A., Ichinohe, Y., Iga, S., Iizuka, R., Ishida, M., Ishihama, N., Ishikawa, K., Ishimura, K., Jaffe, T., Kaastra, J., Kallman, T., Kara, E., Katsuda, S., Kenyon, S., Kimball, M., Kitaguchi, T., Kitamoto, S., Kobayashi, S., Kobayashi, A., Kohmura, T., Kubota, A., Leutenegger, M., Li, M., Lockard, T., Maeda, Y., Markevitch, M., Martz, C., Matsumoto, H., Matsuzaki, K., McCammon, D., McLaughlin, B., McNamara, B., Miko, J., Miller, E., Miller, J., Minesugi, K., Mitani, S., Mitsuishi, I., Mizumoto, M., Mizuno, T., Mukai, K., Murakami, H., Mushotzky, R., Nakajima, H., Nakamura, H., Nakazawa, K., Natsukari, C., Nigo, K., Nishioka, Y., Nobukawa, K., Nobukawa, M., Noda, H., Odaka, H., Ogawa, M., Ohashi, T., Ohno, M., Ohta, M., Okamoto, A., Ota, N., Ozaki, M., Paltani, S., Plucinsky, P., Pottschmidt, K., Sampson, M., Sasaki, T., Sato, K., Sato, R., Sato, T., Sawada, M., Seta, H., Shibano, Y., Shida, M., Shidatsu, M., Shigeto, S., Shinozaki, K., Shirron, P., Simionescu, A., Smith, R., Someya, K., Soong, Y., Sugawara, K., Sugawara, Y., Szymkowiak, A., Takahashi, H., Takeshima, T., Tamagawa, T., Tamura, K., Tanaka, T., Tanimoto, A., Terashima, Y., Tsuboi, Y., Tsujimoto, M., Tsunemi, H., Tsuru, T., Uchida, H., Uchida, Y., Uchiyama, H., Ueda, Y., Uno, S., Vink, J., Watanabe, T., Witthoeft, M., Wolfs, R., Yamada, S., Yamaoka, K., Yamasaki, N., Yamauchi, M., Yamauchi, S., Yanagase, K., Yaqoob, T., Yasuda, S., Yoshida, T., Yoshioka, N., Zhuravleva, I., and Team, X. D., "Status of x-ray imaging and spectroscopy mission (XRISM)," in [*SPACE TELESCOPES AND INSTRUMENTATION 2020: ULTRA-VIOLET TO GAMMA RAY*], DenHerder, J., Nikzad, S., and Nakazawa, K., eds., *Proceedings of SPIE* **11444**, SPIE (2021). Conference on Space Telescopes and Instrumentation - Ultraviolet to Gamma Ray / SPIE Astronomical Telescopes + Instrumentation Conference, DEC 14-18, 2020.

[5] Heilmann, R. K., Bruccoleri, A. R., Kolodziejczak, J., Gaskin, J. A., O'Dell, S. L., Bhatia, R., and Schattenburg, M. L., "Critical-angle x-ray transmission grating spectrometer with extended bandpass and resolving power > 10,000," in [*SPACE TELESCOPES AND INSTRUMENTATION 2016: ULTRAVIOLET TO GAMMA RAY*], DenHerder, J., Takahashi, T., and Bautz, M., eds., *Proceedings of SPIE* **9905**, SPIE (2016). Conference on Space Telescopes and Instrumentation - Ultraviolet to Gamma Ray, Edinburgh, SCOTLAND, JUN 26-JUL 01, 2016.

[6] Heilmann, R. K., Kolodziejczak, J., Bruccoleri, A. R., Gaskin, J. A., and Schattenburg, M. L., "Demonstration of resolving power $\lambda/\Delta\lambda > 10,000$ for a space-based x-ray transmission grating spectrometer," *APPLIED OPTICS* **58**, 1223–1238 (FEB 10 2019).

[7] Heilmann, R. K., Bruccoleri, A. R., Song, J., Cook, M. T., Gregory, J. A., Lambert, R. D., Shapiro, D. A., Young, D. J., Bradshaw, M., Burwitz, V., Hartner, G. D., Langmeier, A., Smith, R. K., and Schattenburg, M. L., "Toward volume manufacturing of high-performance soft x-ray critical-angle transmission gratings," in [*SPACE TELESCOPES AND INSTRUMENTATION 2020: ULTRAVIOLET TO GAMMA RAY*], Den-Herder, J., Nikzad, S., and Nakazawa, K., eds., *Proceedings of SPIE* **11444**, SPIE (2021). Conference on Space Telescopes and Instrumentation - Ultraviolet to Gamma Ray / SPIE Astronomical Telescopes + Instrumentation Conference, DEC 14-18, 2020.

[8] den Herder, J., Brinkman, A., Kahn, S., Branduardi-Raymont, G., Thomsen, K., Aarts, H., Audard, M., Bixler, J., den Boggende, A., Cottam, J., Decker, T., Dubbeldam, L., Erd, C., Goulooze, H., Gudel, M., Guttridge, P., Hailey, C., Al Janabi, K., Kaastra, J., de Korte, P., van Leeuwen, B., Mauche, C., McCalden, A., Mewe, R., Naber, A., Paerels, F., Peterson, J., Rasmussen, A., Rees, K., Sakelliou, I., Sako, M., Spodek, J., Stern, M., Tamura, T., Tandy, J., de Vries, C., Welch, S., and Zehnder, A., "The reflection grating spectrometer on board XMM-Newton," *ASTRONOMY & ASTROPHYSICS* **365**, L7–L17 (JAN 2001).

[9] Canizares, C., Davis, J., Dewey, D., Flanagan, K., Galton, E., Huenemoerder, D., Ishibashi, K., Markert, T., Marshall, H., McGuirk, M., Schattenburg, M., Schulz, N., Smith, H., and Wise, M., "The Chandra high-energy transmission grating: Design, fabrication, ground calibration, and 5 years in flight," *PUBLICATIONS OF THE ASTRONOMICAL SOCIETY OF THE PACIFIC* **117**, 1144–1171 (OCT 2005).

[10] Collon, M. J., Babic, L., Barriere, N. M., Bayerle, A., Castiglione, L., Eenkhoorn, N., Girou, D., Gunther, R., Hauser, E., Jenkins, Y., Landgraf, B., Keek, L., Okma, B., Serrano, G. M., Thete, A., Vacanti, G., Verhoeckx, S., Vervest, M., Voruz, L., Beijersbergen, M. W., Bavdaz, M., Wille, E., Ferreira, I., Fransen, S., Shortt, B., Riekerink, M. O., Haneveld, J., Koelewijn, A., Wijnperle, M., Lankwarden, J.-J., Schurink, B., Start, R., van Baren, C., Hieltjes, P., den Herder, J.-W., Handick, E., Krumrey, M., Bradshaw, M., Burwitz, V., Massahi, S., Svendsen, S., Ferreira, D. D. M., Christensen, F. E., Valsecchi, G., Kailla, G., Mundon, W., Philips, G., and Ball, K., "Silicon pore optics x-ray mirror development for the ATHENA telescope," in [*OPTICS FOR EUV, X-RAY, AND GAMMA-RAY ASTRONOMY X*], ODell, S., Gaskin, J., and Pareschi, G., eds., *Proceedings of SPIE* **11822**, SPIE (2021). Conference on Optics for EUV, X-Ray, and Gamma-Ray Astronomy X, San Diego, CA, AUG 01-05, 2021.

[11] Günther, H. M., Cheimets, P. N., Heilmann, R. K., Smith, R. K., and Collaboration, A., "Performance of a double tilted-rowland-spectrometer on Arcus," in [*UV, X-RAY, AND GAMMA-RAY SPACE INSTRUMENTATION FOR ASTRONOMY XX*], Siegmund, O., ed., *Proceedings of SPIE* **10397**, SPIE (2017). Conference on UV, X-Ray, and Gamma-Ray Space Instrumentation for Astronomy XX, San Diego, CA, AUG 06-08, 2017.

[12] Günther, H. M., DeRoo, C., Heilmann, R. K., Hertz, E., Smith, R. K., Wilms, J., and Collaboration, A., "Ray-tracing Arcus in Phase A," in [*SPACE TELESCOPES AND INSTRUMENTATION 2018: ULTRAVIOLET TO GAMMA RAY*], DenHerder, J., Nikzad, S., and Nakazawa, K., eds., *Proceedings of SPIE* **10699**, SPIE (2018). Conference on Space Telescopes and Instrumentation - Ultraviolet to Gamma Ray, Austin, TX, JUN 10-15, 2018.

[13] Bruccoleri, A., Guan, D., Mukherjee, P., Heilmann, R. K., Schattenburg, M. L., and Vargo, S., "Potassium hydroxide polishing of nanoscale deep reactive-ion etched ultrahigh aspect ratio gratings," *JOURNAL OF VACUUM SCIENCE & TECHNOLOGY B* **31** (NOV 2013).

[14] Heilmann, R. K., Bruccoleri, A. R., Song, J., Levenson, B., Smallshaw, B., Whalen, M., Garner, A., Heine, S. T., Marshall, H. L., Cook, M. T., Gregory, J. A., Lambert, R. D., Shapiro, D. A., Young, D. J., Gullikson, E. M., Nonaka, T., Uchida, A., Quijada, M. A., Hertz, E., Cheimets, P., Smith, R. K., and Schattenburg, M. L., "Manufacture and performance of blazed soft x-ray transmission gratings for Arcus and Lynx," in [*OPTICS FOR EUV, X-RAY, AND GAMMA-RAY ASTRONOMY X*], ODell, S., Gaskin, J., and Pareschi, G., eds., *Proceedings of SPIE* **11822**, SPIE (2021). Conference on Optics for EUV, X-Ray, and Gamma-Ray Astronomy X, San Diego, CA, AUG 01-05, 2021.

[15] Heilmann, R. K., Bruccoleri, A. R., Burwitz, V., deRoo, C., Garner, A., Günther, H. M., Gullikson, E. M., Hartner, G., Hertz, E., Langmeier, A., Müller, T., Rukdee, S., Schmidt, T., Smith, R. K., and Schattenburg, M. L., "X-ray performance of critical-angle transmission grating prototypes for the Arcus mission," *ASTROPHYSICAL JOURNAL* (2022).

[16] Song, J., Heilmann, R. K., Bruccoleri, A. R., and Schattenburg, M. L., "Characterizing profile tilt of nanoscale deep-etched gratings via x-ray diffraction," *JOURNAL OF VACUUM SCIENCE & TECHNOLOGY B* **37** (NOV 2019).

[17] Moharam, M., POMMET, D., GRANN, E., and GAYLORD, T., "Stable implementation of the rigorous coupled-wave analysis for surface-relief gratings - enhanced transmittance matrix approach," *JOURNAL OF THE OPTICAL SOCIETY OF AMERICA A-OPTICS IMAGE SCIENCE AND VISION* **12**, 1077–1086 (MAY 1995). Optical-Society-of-America 2nd Topical Meeting on Diffractive Optics, ROCHESTER, NY, JUN 06-09, 1994.

[18] Heilmann, R. K., Ahn, M., Bruccoleri, A., Chang, C.-H., Gullikson, E. M., Mukherjee, P., and Schattenburg, M. L., "Diffraction efficiency of 200-nm-period critical-angle transmission gratings in the soft x-ray and extreme ultraviolet wavelength bands," *APPLIED OPTICS* **50**, 1364–1373 (APR 1 2011).